

***A block rational Krylov method for
three-dimensional time-domain marine
controlled-source electromagnetic modeling***

Qiu, Changkai and Güttel, Stefan and Ren,
Xiuyan and Yin, Changchun and Liu, Yunhe and Zhang,
Bo and Egbert, Gary

2018

MIMS EPrint: **2018.22**

Manchester Institute for Mathematical Sciences
School of Mathematics

The University of Manchester

Reports available from: <http://eprints.maths.manchester.ac.uk/>

And by contacting: The MIMS Secretary
School of Mathematics
The University of Manchester
Manchester, M13 9PL, UK

ISSN 1749-9097

A block rational Krylov method for three-dimensional time-domain marine controlled-source electromagnetic modelling

Changkai Qiu^{1,2}, Stefan Güttel³, Xiuyan Ren¹, Changchun Yin^{1*}, Yunhe Liu¹, Bo Zhang¹, and Gary Egbert²

¹College of Geo-exploration Science and Technology, Jilin University, Changchun, Jilin, China

²College of Earth, Ocean, and Atmospheric Sciences, Oregon State University, Corvallis, OR, USA

³School of Mathematics, The University of Manchester, Manchester, UK

Running head: Block rational Krylov method

*Corresponding author

E-mail: qiuchangkai@hotmail.com;
stefan.guettel@manchester.ac.uk;
jdrxy@hotmail.com;
yinchangchun@jlu.edu.cn;
liuyunhe@jlu.edu.cn;
em_zhangbo@163.com;
egbert@coas.oregonstate.edu.

February 10, 2019

SUMMARY

We introduce a novel block rational Krylov method to accelerate three-dimensional time-domain marine controlled-source electromagnetic modelling with multiple sources. This method approximates the time-varying electric solutions explicitly in terms of matrix exponential functions. A main attraction is that no time stepping is required, while most of the computational costs are concentrated in constructing a rational Krylov basis. We optimize the shift parameters defining the rational Krylov space with a positive exponential weight function, thereby producing smaller approximation errors at later times and reducing iteration numbers. Furthermore, for multi-source modelling problems, we adopt block Krylov techniques to incorporate all source vectors in a single approximation space. The method is tested on two examples: a layered seafloor model and a 3D hydrocarbon reservoir model with seafloor bathymetry. The modelling results are found to agree very well with those from 1D semi-analytic solutions and finite-element time-domain solutions using a backward Euler scheme, respectively. Numerical benchmarks show that the block method benefits from better memory and cache efficiency, resulting in about 1.26 to 1.48-fold speedup compared to non-block methods. Further efficiency gains are achieved through optimized rational Krylov techniques, allowing our approach to outperform classical time stepping schemes.

Key words: Controlled source electromagnetics (CSEM); Numerical modelling; Marine electromagnetics; Electromagnetic theory.

1 INTRODUCTION

Time-domain electromagnetic (TDEM) surveys are very useful geophysical electromagnetic (EM) techniques for mineral exploration (e.g., [Yang and Oldenburg, 2012](#), [Fountain et al., 2005](#)), hydrocarbon detection (e.g., [Wright et al., 2002](#), [Connell and Key, 2013](#), [Constable, 2010](#), [Constable and Weiss, 2006](#)), hydrogeophysical exploration ([Danielsen et al., 2003](#), [Fitterman and Stewart, 1986](#), [Kafri and Goldman, 2005](#)), and environmental geophysics (e.g., [Hoekstra and Blohm, 1990](#)). The interpretation methods for TDEM data have turned from simple one-dimensional (1D) layered-earth models ([e.g., Farquharson and Oldenburg, 1993](#)) or thin plate models ([Keating and Crossley, 1990](#)) to arbitrarily complicated three-dimensional (3D) models (e.g., [Haber et al., 2004](#), [Oldenburg et al., 2013](#), [Yang et al., 2013](#)) . As forward modelling (and adjoint modelling) routines account for most of the computational runtime during inversion ([Börner, 2010](#)), the availability of accurate and fast three-dimensional TDEM modelling solvers is crucial.

The EM field can be solved in the frequency domain and then transformed to the time domain via the inverse Fourier transform ([Anderson, 1983](#)), Laplace transform ([Stehfest, 1970](#), [Knight and Raiche, 1982](#), [Li et al., 2016](#)), or fast Fourier transform ([e.g., Jang et al., 2013](#)). The main advantage of transform algorithms is that existing integral-equation (e.g., [Cox et al., 2010](#), [Newman et al., 1986](#)), finite-difference ([e.g., Liu and Yin, 2016](#)), and finite-element ([e.g., Li et al., 2017](#)) forward solvers for frequency-domain EM modelling can be readily used to provide the

frequency-domain solutions. One weakness of transform algorithms is difficulties in obtaining accurate EM solutions for high frequencies due to numerical dispersion, which may lead to inaccurate results at early time channels. In addition, inverse Fourier transform-based methods ([Anderson, 1983](#)) need dozens of EM solutions for a rather wide frequency band, while for inverse Laplace transform, Laplace-domain responses must be recomputed for each sampled time channel, which are both computationally expensive.

It is more straightforward to perform the numerical computations directly in the time domain. The space discretization of the time-dependent electric curl-curl equation results in an initial value problem for the electric field. Explicit and implicit time-stepping methods have been widely employed for the solution of such initial value problems. Explicit methods calculate the solutions at the current time step from the solutions at a few (depending on the order of the difference method) earlier time steps. Compared with implicit methods, explicit methods are easy to implement and parallelize, and the computational cost per time step is relatively low. However, many problems arising from geophysical electromagnetics are very stiff ([Ascher and Petzold, 1998](#), [Haber *et al.*, 2002](#), [Haber *et al.*, 2004](#)), for which the use of an explicit method requires impractically small time steps to keep the error acceptable. For example, the initial time step for the Du Fort-Frankel finite-difference scheme ([Du Fort and Frankel, 1953](#)) must be constrained (see e.g., [Wang and Hohmann, 1993](#), [Commer and Newman, 2004](#), [Oristaglio and Hohmann, 1984](#)) to prevent the artificial

displacement current term ([Chew, 1995](#)) from dominating the EM diffusion, which leads to extremely small initial time steps and further makes explicit schemes inefficient for long time intervals.

Compared to explicit methods, implicit methods involve the solution of system equations at the current time step and the later ones, making their computational cost per time step relatively high. The backward Euler (BE) scheme is a widely used implicit method to advance the EM solution in time, which is unconditionally stable, regardless of the choice of time step Δt ([Um et al., 2010](#), [Ascher and Petzold, 1998](#)).

For such problems, to achieve a given accuracy, it takes much less computational time to use an implicit method with larger time steps, even taking into account that one needs to solve a linear system of equations at each time step. Furthermore, the BE method can strongly attenuate high frequencies of the error ([Haber et al., 2002](#)). Due to the obvious advantages mentioned, the BE scheme has lately received great attention in the application to TDEM modelling over the past decades (e.g., [Haber et al., 2002](#), [Um et al., 2010](#), [Yin et al., 2016a](#), [Yin et al., 2016b](#), [Cai et al., 2017](#), [Ren et al., 2017](#)). However, for BE schemes, solving hundreds (see e.g., [Um et al., 2010](#), [Yin et al., 2016b](#)) of linear systems are still very expensive, although the computational cost could be reduced if implemented with direct solvers. In addition, time-stepping sizes (include the initial time step and the time-stepping multiplier) must be carefully selected taking into account the accuracy. Using larger time steps (and less number of time steps) will definitely accelerate the TDEM modelling, while larger errors will be

observed once the time-stepping size is increased unreasonably, which have been reported as periodic oscillations for airborne and ground TDEM problems by [Yin et al. \(2016b\)](#) and [Li et al. \(2018\)](#).

In this work, we will use rational Krylov methods for solving the initial value problem stated above. Polynomial and rational Krylov methods have been widely used for the approximation of matrix functions, such as the matrix exponential, and in the context of geophysical modelling. [Druskin and Knizhnerman \(1988\)](#) suggested to solve the nonstationary problems of electric prospecting by the spectral Lanczos decomposition method, which utilizes a polynomial Krylov space to approximate the action of a matrix exponential onto a vector. They further proposed to use this polynomial Krylov approach for Maxwell's equations in both time and frequency domains ([Druskin and Knizhnerman, 1994](#)). A rational Krylov variant of this method was first adopted by [Druskin et al. \(2009\)](#) to simulate the TDEM problem. The choice of shifts in the procedure for constructing the rational Krylov basis was further discussed by [Druskin et al. \(2010\)](#). The Cole-Cole model was considered in 3D TDEM modelling with a rational Krylov method to take into account the induced-polarization effects by [Zaslavsky et al. \(2011\)](#). Furthermore, [Börner et al. \(2008\)](#) presented a shift-and-invert Krylov method to solve the 3D Maxwell equations using a finite-element discretization in the frequency domain, while the time-domain responses were then evaluated by fast Hankel transform. More recently, [Börner et al. \(2015\)](#) applied a rational Krylov method to the problem of direct TDEM modelling,

while exploiting repeated shift parameters with a direct solver to compute the basis vectors in the Krylov space, which saves significant time compared to the frequency-domain to time-domain transform scheme. In addition, block Krylov techniques for CSEM problems with multiple right-hand sides have been investigated by [Puzyrev and Cela \(2015\)](#), with fewer iteration numbers and reduced computational time being observed for block methods.

In this paper, we introduce a block rational Krylov method for multi-source time-domain CSEM problems and improve the multi-source modelling in two ways. First, the use of block Krylov techniques which contain all the source vectors in the same approximation space results in better utilization of Level-3 Basic Linear Algebra Subprograms (BLAS) routines, thereby resulting in a better cache utilization and higher floating-point operations per communication ratio. Secondly, we propose a new approach to the shift parameters optimization, extending the work in [Börner *et al.* \(2015\)](#) by incorporating a weight function taking into account the exponential decays of the transient EM field. These results in smaller iteration numbers of the block method compared to the uniform approximated error optimization, further reducing the time to solution.

The rest of the paper is organized as follows. We first introduce how to discretize the electric field wave equation in space with the vector basis function on an unstructured tetrahedral grid, and recall the typical backward Euler scheme used in finite-element time-domain (FETD) methods. Then we show that the EM solutions

can be represented as the product of a matrix exponential function with a vector, which do not need any time stepping. Theoretical details are devoted to how to solve the matrix-vector function via block rational Krylov method for multiple sources. Even though the general method works for TDEM with magnetic-loop sources or electric-dipole sources, we only take time-domain marine CSEM as examples to prove its correctness. After the methodology part, we verify the accuracy of our method via a 1D layered space model. At last, a complicated 3D hydrocarbon reservoir model with seafloor bathymetry is adopted to fully benchmark the block rational Krylov method.

2 METHODOLOGY

2.1 Governing equation and finite-element discretization in space

Starting from the time-dependent Maxwell's equations in the differential form and eliminating the magnetic field, we can obtain the electric field curl-curl equation inside the modelling domain Ω :

$$\nabla \times \left[\frac{1}{\mu} \nabla \times \mathbf{E}(\mathbf{r}, t) \right] + \sigma \frac{\partial \mathbf{E}(\mathbf{r}, t)}{\partial t} = - \frac{\partial \mathbf{J}_s(t)}{\partial t}, \quad (1.)$$

where the displacement current is neglected, $\mathbf{E}(\mathbf{r}, t)$ is the electric field at time t , \mathbf{r} is the position vector, μ is the magnetic permeability, σ is the electrical conductivity, and $\mathbf{J}_s(t)$ is the electric current density of the imposed electromagnetic source.

To discretize eq. (1.) using finite elements, we define a residual vector $\mathbf{R}(\mathbf{r}, t)$ as:

$$\mathbf{R}(\mathbf{r}, t) = \nabla \times \left[\frac{1}{\mu} \nabla \times \mathbf{E}(\mathbf{r}, t) \right] + \sigma \frac{\partial \mathbf{E}(\mathbf{r}, t)}{\partial t} + \frac{\partial \mathbf{J}_s(t)}{\partial t}. \quad (2.)$$

Following the Galerkin's method, we minimize the residual vector $\mathbf{R}(\mathbf{r},t)$ in a weighted-integral sense

$$\iiint_{\Omega} \mathbf{N}(\mathbf{r}) \mathbf{R}(\mathbf{r},t) d\nu = 0, \quad (3.)$$

where the vector basis functions $\mathbf{N}(\mathbf{r})$ are chosen as the weighted basis sets. The modelling domain is divided into a set of tetrahedral elements by the mesh generator first. Nédélec H(curl)-conforming vector basis functions defined in the Sobolev spaces ([Nédélec, 1980](#)) are used to approximate the electric field for each element because they meet the continuity condition of tangential electric field and automatically satisfy that the divergence of the electric field is zero. For each tetrahedral element, the electric field can be written as

$$\mathbf{E}(\mathbf{r},t) = \sum_{i=1}^{i=6} e_i(t) \mathbf{N}_i(\mathbf{r}), \quad (4.)$$

where $e_i(t)$ is the electric field at time t for the i -th local edge in this element.

Substituting eq. (2.) and eq. (4.) into eq. (3.), integrating by parts and moving the source term of eq. (2.) to the right side, then we can obtain

$$\mathbf{A}\mathbf{E}(t) + \mathbf{B} \frac{d\mathbf{E}(t)}{dt} = \mathbf{S}, \quad (5.)$$

where \mathbf{A} , \mathbf{B} and \mathbf{S} are the global stiffness matrix, mass matrix and source term, respectively. Their local forms for each tetrahedral element are denoted with a superscript “e” and are defined as:

$$\mathbf{A}_{ij}^e = \frac{1}{\mu} \iiint_{\Omega^e} (\nabla \times \mathbf{N}_i) \cdot (\nabla \times \mathbf{N}_j) d\nu, \quad (6.)$$

$$\mathbf{B}_{ij}^e = \iiint_{\Omega^e} (\mathbf{N}_i \cdot \boldsymbol{\sigma} \cdot \mathbf{N}_j) d\nu, \quad (7.)$$

$$\mathbf{S}_i^e = - \iiint_{\Omega^e} \left(\mathbf{N}_i \cdot \frac{\partial \mathbf{J}_s(t)}{\partial t} \right) d\nu. \quad (8.)$$

The imposed current source term $\mathbf{J}_s(t)$ is considered as an electric dipole in the elements which contain a segment of transmitter, and elsewhere it is zero ([Yin et al., 2016b](#), [Li et al., 2017](#), [Jahandari and Farquharson, 2014](#))

$$\mathbf{J}_s^e(t) = \mathbf{I}^e(t)\delta(\mathbf{r} - \mathbf{r}_0)dl, \quad (9.)$$

where $\mathbf{I}^e(t)$ is the imposed current density in this element, \mathbf{r}_0 is the coordinate of the midpoint of the small approximated electric dipole, dl is the length of the dipole, and δ is the Dirac delta function. Substituting eq. (9.) into eq. (8.) and considering the integral property of the delta function, the source term for each element is

$$\mathbf{S}_i^e = -\mathbf{N}_i(\mathbf{r}_0)\frac{d\mathbf{I}^e(t)}{dt}dl. \quad (10.)$$

2.2 Boundary conditions and initial conditions

The unstructured tetrahedral grids allow efficient local refinements in the region with high gradients of EM field. In addition, increasing the domain size by stretching elements far from the central sensitive domain does not result in a significant increase of the total number of elements. When generating the grid, we always refine the central sensitive domain, which contains the EM sources and receivers, while extending the outer boundaries of the model far away from the sensitive domain, such that both the tangential electric field $\mathbf{E}(\mathbf{r},t)$ and normal magnetic-induction time-derivative components $\frac{\partial \mathbf{H}(\mathbf{r},t)}{\partial t}$ are zero on the outer boundary. To obtain a unique numerical solution for a specific model using eq. (5.), homogeneous Dirichlet boundary conditions are incorporated on the outer boundary $\partial\Omega$ of the entire modelling domain Ω :

$$[\mathbf{n} \times \mathbf{E}(\mathbf{r}, t)]_{\partial\Omega} = 0, \quad (11.)$$

where \mathbf{n} is the normal vector for the surfaces on $\partial\Omega$.

For the time-dependent problem, we also need to set up the initial conditions at the time $t=0$. The initial electric field can be decomposed into two parts ([Commer and Newman, 2004](#), [Um et al., 2010](#))

$$\mathbf{E}_{\text{initial}} = \mathbf{E}_{\text{source}} + \mathbf{E}_{\text{DC}}. \quad (12.)$$

where $\mathbf{E}_{\text{source}}$ is the electric field defined by the imposed source and \mathbf{E}_{DC} is the direct-current (DC) electric field induced by the electrodes of EM transmitter. \mathbf{E}_{DC} vanishes for a magnetic loop source. However, for an electric source excited by a step-off waveform, there exists a DC electric field all over the modelling domain. The electric field \mathbf{E}_{DC} for each edge is calculated from the potentials $\phi(\mathbf{r})$ at the two nodes of this edge. Therefore, we solve a direct current problem to compute the electric potentials for all the nodes in the grid, which satisfies the following 3D Poisson equation

$$\nabla \cdot (\sigma \nabla \phi(\mathbf{r})) = -\nabla \cdot \mathbf{j}_s(\mathbf{r}). \quad (13.)$$

Eq. (13.) is solved using a total-potential approach on the same grid as the time-domain problem. The source term for the DC problem is zero except at the two electrodes of the CSEM transmitter. Here the homogenous Dirichlet boundary conditions are considered in the scalar finite-element discretization for the DC problem, which is consistent with the boundary condition for the time-domain problem.

2.3 Backward Euler scheme for discretization in time

The solution of eq. (5.), eq. (11.) and eq. (12.) can be advanced in time by the implicit backward Euler scheme. For the second-order backward Euler scheme, the difference of electric field at the $i+2^{\text{th}}$ time step can be approximated by

$$\frac{d\mathbf{E}^{(i+2)}(t)}{dt} = \frac{1}{2\Delta t} [3\mathbf{E}^{(i+2)}(t) - 4\mathbf{E}^{(i+1)}(t) + \mathbf{E}^{(i)}(t)], \quad (14.)$$

where $\mathbf{E}^{(i+1)}(t)$ and $\mathbf{E}^{(i+2)}(t)$ are the electric field at the $i+1^{\text{th}}$ and $i+2^{\text{th}}$ time step respectively. Applying eq. (14.) to eq. (5.) yields

$$(3\mathbf{B} + 2\Delta t\mathbf{A})\mathbf{E}^{(i+2)}(t) = \mathbf{B}[4\mathbf{E}^{(i+1)}(t) - \mathbf{E}^{(i)}(t)] + 2\Delta t\mathbf{S}^{(i+2)}. \quad (15.)$$

We can thus solve eq. (15.) at each time step to obtain the transient electric field, and simultaneously compute the time-varying magnetic fields using Faraday's law.

2.4 Explicit electric solutions in terms of matrix functions

The main idea behind the (block) rational Krylov method is that we can obtain the explicit solution to the initial value problem defined by eq. (5.) directly as the product of a matrix exponential function with a vector ([Börner et al., 2015](#))

$$\mathbf{E}(t) = \exp(-t\mathbf{B}^{-1}\mathbf{A})\mathbf{B}^{-1}\mathbf{s} = f^t(\mathbf{M})\mathbf{b}, \quad (16.)$$

where

$$\mathbf{M} = \mathbf{B}^{-1}\mathbf{A}, \mathbf{b} = \mathbf{B}^{-1}\mathbf{s}. \quad (17.)$$

Here $\mathbf{s} = \mathbf{S} + \mathbf{B}\mathbf{E}_{\text{DC}}$ is the initial current density. The function $f^t(\mathbf{z})$ in eq. (16.) is

$$f^t(\mathbf{z}) = \exp(-t\mathbf{z}). \quad (18.)$$

Once the global stiffness matrix \mathbf{A} , mass matrix \mathbf{B} and source term \mathbf{s} are assembled from their local forms, we solve the equation $\mathbf{B}\mathbf{b} = \mathbf{s}$ via a direct solver to

calculate the vector \mathbf{b} . For the multi-source problem, \mathbf{b} is a collection of vectors \mathbf{b}_i

$$\mathbf{b} = [\mathbf{b}_1, \mathbf{b}_2, \dots, \mathbf{b}_{ns}], \quad (19.)$$

where ns is the number of sources and \mathbf{b}_i is the i -th source vector computed from eq. (17.).

2.5 A block rational Krylov algorithm for multi-source modelling

The matrices arising from geophysical EM modelling are typically large and sparse, and usually it is impractical to compute the (generally dense) matrix function $\exp(-t\mathbf{M})$ first and then perform the matrix-vector product with the vector \mathbf{b} . Krylov methods avoid this problem by approximating the product $\exp(-t\mathbf{M})\mathbf{b}$ directly via projection onto a Krylov space, without any time stepping.

In order to introduce the basic concept of rational Krylov spaces, and to motivate their use compared with the more familiar time-stepping methods, let us consider the solution of the initial value problem at a time point t using m steps of the basic first-order backward Euler scheme with step size $\tau = t/m$: $\mathbf{E}_i = (\mathbf{I} + \tau\mathbf{M})^{-1}\mathbf{E}_{i-1}$, $i = 1, 2, \dots, m$, where \mathbf{I} is the identity matrix. Note that \mathbf{E}_i is the time-stepping approximation for $\mathbf{E}(t)$. Crucially, we have $\mathbf{E}_m = (\mathbf{I} + \tau\mathbf{M})^{-m}\mathbf{b}$, which shows that the backward Euler method produces a result $\mathbf{E}_m = r(\mathbf{M})\mathbf{b}$ where $r(z) = (1 + \tau z)^{-m}$ is a rational function with a pole of multiplicity m at $z = -1/\tau$. The reasoning behind rational Krylov methods is to replace $r(z)$ with a potentially better rational function by seeking approximations to $\mathbf{E}(t)$ from an m -dimensional *rational Krylov space* $Q_m(\mathbf{M}, \mathbf{b}) = q_m(\mathbf{M})^{-1} \text{span}\{\mathbf{b}, \mathbf{M}\mathbf{b}, \dots, \mathbf{M}^{m-1}\mathbf{b}\}$ where $q_m(z)$ is a

polynomial of degree at most m , having no root at any of the eigenvalues of \mathbf{M} (otherwise, $q_m(\mathbf{M})$ would not be invertible). The roots of $q_m(z)$ are often referred to as the *poles* or *shift parameters* of the rational Krylov space. Note that $Q_m(\mathbf{M}, \mathbf{b})$ is a linear space of rational functions $r(\mathbf{M})\mathbf{b}$, all having the same denominator $q_m(z)$. In particular, if we choose $q_m(z) = (1 + \tau z)^m$, then our backward Euler approximation \mathbf{E}_m is an element of $Q_m(\mathbf{M}, \mathbf{b})$. If, on the other hand, $q_m(z)$ is chosen as the constant polynomial $q_m(z) = 1$, then $Q_m(\mathbf{M}, \mathbf{b})$ is just a polynomial Krylov space. Such spaces are widely used for the solution of linear systems, for example in the CG or GMRES methods ([Saad, 2003](#)). As we will show later, the choice of $q_m(z)$, i.e., the shift parameters, plays a crucial role when tuning the space $Q_m(\mathbf{M}, \mathbf{b})$ so that it contains good approximations to $\exp(-t\mathbf{M})\mathbf{b}$.

Polynomial Krylov methods have become very popular since the 1990s for approximating $f^t(\mathbf{M})\mathbf{b}$, the action of matrix functions $f^t(\mathbf{M})$ onto a (single) vector \mathbf{b} and are still a topic of recent research; see e.g. ([Saad, 1992](#), [Druskin and Knizhnerman, 1994](#), [Frommer et al., 2014](#)). The polynomial based techniques are explicit essentially for the fact that solving linear system equations are not required, thus they are not suitable for very stiffness problems ([Galloupolos and Saad, 1989](#)). Rational Krylov methods are the natural extension of these approaches to rational approximants, based on rational Krylov spaces ([Ruhe, 1994](#), [Van den Eshof and Hochbruck, 2006](#), [Moret and Novati, 2004](#), [Druskin et al., 2009](#)). For a review of rational Krylov techniques and the various approaches to choose the involved shift

parameters in a (near-) optimal way, see [Güttel \(2013\)](#).

To approximate the matrix functions $f^t(\mathbf{M})\mathbf{b}$ with a block vector, we can either apply the rational Arnoldi method with each column \mathbf{b}_i separately (herein referred to as single-vector rational Krylov method), or we can treat all columns of \mathbf{b} at once as a block (block rational Krylov method). The block rational Arnoldi algorithm is the natural extension of Ruhe's original algorithm ([Ruhe, 1994](#)) to the block case. In our application of rational Krylov method, the inner product is induced by the mass matrix \mathbf{B} , i.e., $\langle \mathbf{x}, \mathbf{y} \rangle_{\mathbf{B}} = \mathbf{y}^H \mathbf{B} \mathbf{x}$, while the induced norm $\|\mathbf{x}\|_{\mathbf{B}} = \sqrt{\mathbf{x}^H \mathbf{B} \mathbf{x}}$. Given a starting block vector \mathbf{b} and a sequence of shifts $\xi_1, \xi_2, \dots, \xi_m$, the block rational Arnoldi algorithm uses Gram-Schmidt orthogonalisation to compute a sequence of block vectors $\mathbf{v}_1, \mathbf{v}_2, \dots, \mathbf{v}_{m+1}$ spanning a rational Krylov space and being mutually \mathbf{B} -orthonormal, i.e., $\mathbf{v}_i^T \cdot \mathbf{B} \cdot \mathbf{v}_j = \mathbf{0}$ whenever $i \neq j$ and $\mathbf{v}_i^T \cdot \mathbf{B} \cdot \mathbf{v}_i = \mathbf{I}$, where \mathbf{O} and \mathbf{I} is the $ns \times ns$ zero and identity matrix respectively. The shifts $\xi_1, \xi_2, \dots, \xi_m$ are important parameters, the choice of which influence both the computational cost of the algorithm and the approximation quality of the rational Arnoldi approximation defined below, where we will also discuss the choice of the shift parameters tailored to our application. For consistency purposes, the algorithm for single-vector rational and block rational Krylov methods is summarized as follows:

Algorithm 1: Block rational Arnoldi algorithm

Input: Finite-element global matrices \mathbf{A} , \mathbf{B} , source vector \mathbf{b} of full rank, shift parameters $\xi_1, \xi_2, \dots, \xi_m$

Output: \mathbf{B} -orthonormal block Krylov basis $\mathbf{V}_{m+1} := [\mathbf{v}_1, \mathbf{v}_2, \dots, \mathbf{v}_{m+1}]$

- 1 **Compute** $\mathbf{v}_1 = \mathbf{b}\mathbf{R}_1^{-1}$, where $\mathbf{b} = \mathbf{v}_1\mathbf{R}_1$ is a thin QR factorization
- 2 **for** $j = 1, \dots, m$
- 3 **Solve** $\mathbf{w}_j = (\mathbf{A} - \xi_j \mathbf{B})^{-1} \mathbf{B} \mathbf{v}_j$
- 4 **Orthogonalize** $\mathbf{w}_j = \mathbf{w}_j - \sum_{i=1}^{i=j} \mathbf{v}_i \mathbf{h}_j$, where $\mathbf{h}_j = \mathbf{v}_i^T \cdot \mathbf{B} \cdot \mathbf{w}_j$
- 5 **Compute** $\mathbf{v}_{j+1} = \mathbf{w}_j \mathbf{R}_{j+1}^{-1}$, where $\mathbf{w}_j = \mathbf{v}_{j+1} \mathbf{R}_{j+1}$ is a thin QR factorization
- 6 **end**

In the case of just a single source, $ns=1$, the normalization steps $\mathbf{v}_{j+1} = \mathbf{w}_j \mathbf{R}_{j+1}^{-1}$ reduce to computing $\mathbf{v}_{j+1} = \mathbf{w}_j / \|\mathbf{w}_j\|_{\mathbf{B}}$. Note that the QR factorizations must also be performed in the inner product induced by the matrix \mathbf{B} so that $\mathbf{v}_i^T \cdot \mathbf{B} \cdot \mathbf{v}_j = \mathbf{I}$. This can be achieved most easily by applying the Gram-Schmidt orthogonalisation procedure to the columns of the blocks \mathbf{w}_j , using the \mathbf{B} inner product. Note that we have implicitly assumed that all factors \mathbf{R}_j are invertible, i.e., we assume that all block vectors \mathbf{w}_j are of full column rank ns . The case when a block vector \mathbf{w}_j becomes (nearly) rank deficient can be detected in practice by (numerically) singular factor \mathbf{R}_j and is treated by removing (nearly) linearly dependent columns from the rational Krylov basis. This procedure is known as *deflation* and is implemented in the block rational Arnoldi algorithm of the Rational Krylov Toolbox ([Berljafa et al., 2014](#)) that we use for our numerical computations. For our case of EM modelling, we did not observe any deflation effects due to the fact that our source vectors are

linearly independent.

When the algorithm completes, the returned basis matrix $\mathbf{V}_{m+1} = [\mathbf{v}_1, \mathbf{v}_2, \dots, \mathbf{v}_{m+1}]$ is \mathbf{B} -orthonormal, i.e., $\mathbf{V}_{m+1}^T \mathbf{B} \mathbf{V}_{m+1} = \mathbf{I}$. The rational Arnoldi approximation to the electric field $\mathbf{E}(t)$ is then obtained as follows:

$$\mathbf{E}_{\text{Arnoldi}}(t) = \mathbf{V}_{m+1} \exp(-t\mathbf{A}_{m+1}) \mathbf{V}_{m+1}^T \mathbf{B} \mathbf{b}, \quad (20.)$$

where $\mathbf{A}_{m+1} = \mathbf{V}_{m+1}^T \mathbf{A} \mathbf{V}_{m+1}$ projects the matrix \mathbf{A} onto the subspace with respect to the subspace basis \mathbf{V}_{m+1} .

The total number of rational Arnoldi iterations, i.e., m , is usually small (in our case, in the order of at 40). Therefore the matrix \mathbf{A}_{m+1} is of moderate size ($m+1$) $\times ns$ and the computation of its exponential $\exp(-t\mathbf{A}_{m+1})$ is typically of negligible cost compared to the computation of the rational Krylov basis \mathbf{V}_{m+1} . Fortunately, the expensive computation of this basis \mathbf{V}_{m+1} is only performed once and independent of the number of time points t where we want to evaluate eq. (20.). The time dependence when evaluating approximated electric field solution with the rational Krylov basis \mathbf{V}_{m+1} is fully concentrated in $\exp(-t\mathbf{A}_{m+1})$. The computationally most expensive operation per rational Arnoldi iteration is the linear system solve for \mathbf{w}_j with the coefficient matrix $(\mathbf{A} - \xi_j \mathbf{B})$. However, in our case the shifts ξ_j will be chosen constant over several iterations so that the matrix factorizations of the direct solver can be reused. This is similar to what has been advocated in [Börner et al. \(2015\)](#) for the non-block Krylov case.

The use of block techniques here could result in better computational

performance for problems with moderate number of sources ns . As solving the linear system $\mathbf{w}_{j+1} = (\mathbf{A} - \xi_j \mathbf{B})^{-1} \mathbf{Bv}_j$ and the operations \mathbf{Bv}_j , $\mathbf{v}_i \mathbf{h}_j$, and $\mathbf{h}_j = \mathbf{v}_i^T \mathbf{Bw}_{j+1}$ are performed for all ns block columns simultaneously, the block methods require less memory access to the stored decomposition results and matrices. On the other hand, when running the onetime matrix-matrix multiplication instead of several matrix-vector products, the method makes good use of Level 3 BLAS for matrix-matrix operations. These lead to better cache utilization and higher floating-point operations per communication ratio. However, as the block matrix operations are non-linear time complexity with respect to the number of columns ns , the computational cost may increase dramatically when more source vectors are added, thereby eliminating the performance gains.

Choice of shift parameters

Similarly to what has been proposed in [Börner et al. \(2015\)](#) we find negative shift parameters $\xi_1, \xi_2, \dots, \xi_m$ as the (repeated) roots of a polynomial defined as $q_m(z) = (z - \mu_1)^d (z - \mu_2)^d \dots (z - \mu_p)^d$ by solving a surrogate approximation problem using the rational Arnoldi method itself. The subscript p denotes the number of distinct (repeated) roots of the polynomial $q_m(z)$ of degree m , while the superscript d is the number of repetitions of each pole, hence $q \times d = m$. [Börner et al. \(2015\)](#) found that using $p = 2$ cyclically repeated shifts seems to be the most efficient in the application to TDEM. In other words, for a given number m of rational Krylov iterations, repeating $p = 2$ shifts for $d = m/2$ times results in a good trade-off

between the number of matrix factorizations and the approximation quality of the rational Arnoldi approximants.

More precisely, we set the surrogate matrix $\bar{\mathbf{M}} = \text{diag}(\lambda_1, \lambda_2, \dots, \lambda_n)$ and vector $\bar{\mathbf{b}} = [1, 1, \dots, 1]^T$, with the eigenvalues $\lambda_j \geq 0$ chosen dense enough to mimic a continuous spectrum. In our case, we choose 1000 logarithmically spaced points in the spectral interval $[10^{-6}, 10^6]$. We found this choice sufficient in the sense that the computed shift parameters did not change significantly when using more than a thousand points or longer spectral intervals. Given positive integers p and d , and an initial guess for negative shift parameters $\mu_1, \mu_2, \dots, \mu_p < 0$, we try to minimize the worst-case error

$$\text{Err}(\mu_1, \mu_2, \dots, \mu_p) = \max_{t_{\min} \leq t \leq t_{\max}} \max_{z \geq 0} w(t) \|\exp(-t\bar{\mathbf{M}})\bar{\mathbf{b}} - \mathbf{E}_{\text{Arnoldi}}(t)\|_2. \quad (21.)$$

The parameters $\mu_1, \mu_2, \dots, \mu_p$ which approximately minimize $\text{Err}(\mu_1, \mu_2, \dots, \mu_p)$ give good choices for the shifts in the rational Arnoldi algorithm ([Börner et al., 2015](#)). Note that the weight function $w(t)$ does not appear in that work, but we found it necessary for cases which the transient electromagnetic field varies over rather large orders of magnitude. This happens in particular for long time intervals $[t_{\min}, t_{\max}]$, or when the model is very resistive and the electromagnetic field decays quickly. Choosing $w(t)$ as a positive function allows us to place more weight on later time t (as $\|\exp(-t\bar{\mathbf{M}})\bar{\mathbf{b}}\|_2$ decays exponentially when t increases). In our experiments we choose $w(t) = \exp(\alpha t)$ with an appropriately chosen $\alpha > 0$.

To illustrate the above discussion at the example of time-domain marine CSEM

modelling, we consider a time interval $t = [10^{-2}, 10^2]\text{s}$ and set $\alpha = 0.1$. As shown in Fig. 1(a), this produces a weight function $w(t) = \exp(\alpha t)$ which increases from 1 to 22004 on $t = [10^{-2}, 10^2]\text{s}$, approximately corresponding to the three to four orders of decay of the transients in typical marine CSEM models. We now perform a total of $m=40$ rational Arnoldi iterations with two distinct shifts for the surrogate model, finally the two optimal shifts obtained by the parameter search procedure (i.e., eq. (21)) are $\xi_1 = -0.1654$ and $\xi_2 = -76.3031$. The error curve of the surrogate rational Arnoldi approximation, evaluated for 100 time points in $t = [10^{-2}, 10^2]\text{s}$, is shown in Fig. 1(b). Note how the error decays for late time points, staying below the inverse of the scaled weight function (the dashed black curve). We also show in red the error orthogonal projection of the exact exponential $\exp(-t\bar{\mathbf{M}})\bar{\mathbf{b}}$ onto the rational Krylov space. The fact that this error curve is very close to the rational Arnoldi curve is an illustration of the near-optimality of the rational Arnoldi approximation; see e.g. [Güttel \(2013\)](#)[Corollary 3.4].

2.6 Analysis of error

The numerical errors involved in computing the rational Arnoldi approximation $\mathbf{E}_{\text{Arnoldi}}(t)$ fall into three classes. The first error source is due to the spatial discretization, i.e., model setup, mesh generation, and the finite-element approximation, including solving the DC problem for the initial conditions and using the Nédélec vector basis functions to solve for the electric field. This approximation error is inherent to the finite element method, but can be controlled and reduced with

carefully designed high-quality meshes. For a detailed analysis we refer to [Ren *et al.* \(2013\)](#). The second error source is the Arnoldi approximation $\mathbf{E}_{\text{Arnoldi}}(t)$ over the time interval of interest. Here the most important factor is the choice of shift parameters. As we have illustrated in Fig. 1, our shift strategy results in a uniform error $w(t)\|\exp(-t\bar{\mathbf{M}})\bar{\mathbf{b}}\|_2$ over the relevant time interval for the surrogate approximation problem. The accuracy of $\mathbf{E}_{\text{Arnoldi}}(t)$ as an approximation to the original is limited by the accuracy of the surrogate problem. As proved by [Börner *et al.* \(2015\)](#) and [Güttel \(2013\)](#), this shift strategy leads to convergence independent of mesh size and conductivity structure, resulting in exponentially decaying error for arbitrary models. (A mesh refinement or change in conductivity structure merely affects the spectral interval of \mathbf{M} , and the robust convergence is a simple consequence of the fact that the shift optimization has been performed for an unbounded spectral interval.) For FETD using second-order BE schemes, on the other hand, the second error source is owing to the local truncation error $o(\Delta t^3)$ of time discretization, which usually demonstrates as a periodic oscillation because we increase the time steps after a fixed number of iterations. The final error source is the numerical solution of the linear systems in Algorithm 1 and the construction of the **B**-orthonormal block Krylov basis. These errors, due to numerical round-off, are usually of much smaller size relative to the inaccuracies introduced by the first two error classes.

3 NUMERICAL EXPERIMENTS

The finite-element discretization and backward Euler scheme are implemented in modern Fortran. The open source tetrahedral mesh generator TetGen ([Si, 2015](#)) is applied to recover the topology information of the mesh. Meanwhile, we use the sparse direct solver MUMPS ([Amestoy et al., 2006](#)) of version 5.1.2 with the ordering package PORD ([Schulze, 2001](#)) for BE schemes in FETD. The MATLAB implementation of block rational Arnoldi algorithm in the Rational Krylov Toolbox ([Berljafa et al., 2014](#)) is used for computing the rational Krylov bases. Due to the symmetry of the stiffness and mass matrices arising from finite-element discretization, we only factorize the upper triangle part of the matrices instead of the entire ones in FETD or rational Krylov methods. All our numerical experiments are performed on a Windows (R) workstation equipped with two Intel (R) Xeon (R) CPU E5-2650 v2 @ 2.60 GHz and 128 GB of memory.

In this section, we compare the proposed block rational Krylov method with the BE schemes for CSEM modelling to evaluate its accuracy and performance. As the time stepping in BE schemes affects the results accuracy and dominates the main computation cost in FETD method, we first determine the time steps. As shown in Fig. 2, three different time-stepping schemes are designed with the total number of time steps 1000, 595 and 200 respectively. The initial time step size is chosen as 10^{-3} s and the time step Δt increases at a fixed multiplier. The time-stepping increasing procedures are nine, six and four times for the three schemes. Therefore, comparisons with these three time-stepping schemes can illustrate a comprehensive view of the

efficiency of our block rational Krylov method.

3.1 A layered seafloor model

Accuracy verification

To verify the validity and accuracy of the block rational Krylov algorithm for multi-source time-domain CSEM modelling, we first consider a moving CSEM transmitter over a two-layered seafloor. The depth of the seawater is 1000 m. The conductivities of seawater and seafloor sediments are 3.33 S/m and 1.428 S/m respectively, while the conductivity of air is set to 10^{-8} S/m. The EM transmitter is an electric dipole with a finite length of 250 m, which is placed 100 m above the seafloor. To clearly discuss the problem, we conduct the forward modelling with only three sources that are located at $x=0$ m, 1000 m and 2000 m respectively, where 8 receivers with a space of 1000 m are placed on the seafloor, as shown in Fig. 3.

The outer boundary of the grid for this layered model is empirically set 50 km from the origin, which can satisfy the Dirichlet boundary condition. Fig. 4 illustrates the cross section of the tetrahedral grid at $y=0$ m. Each transmitter is divided into 50 segments, moreover the elements near the transmitters and receivers are locally refined, and generating a grid consists of 173,790 tetrahedral elements and 29,609 nodes. Consequently, the total number of unknowns is 204,229.

Fig. 5 shows the inline electric field E_x and vertical electric field E_z from the block rational Arnoldi approximation of order $m=40$, and their relative errors with respect to the 1D semi-analytic solutions. The 1D time-domain results are obtained via an

inverse Fourier transform from frequency-domain solutions ([Schmucker and Weidelt, 1975](#)). The CSEM responses for the fixed-offset transmitter-receiver pairs at same depth should be identical for a layered model. From Fig. 5(a) and Fig. 5(c), it is clearly seen that both E_x and E_z are nearly identical at three different offsets, and the block rational Krylov solutions agree well with the 1D solutions for the three sources. Although the relative errors for E_x increase at very late time channels, the maximum relative errors are still less than 2.5% (cf. Fig. 5(b)). The comparison of Fig. 5(c) with Fig. 5(a) further indicates that the vertical component E_z is an order of magnitude smaller than E_x for a horizontal electric dipole in the sea water, which implies that E_z is more sensitive to the numerical errors. This coincides well with Fig. 5(d) that the relative errors for E_z are larger than E_x , and the errors become about 6% at late times, while it is still acceptable for 3D forward modelling. The relative errors between block rational Krylov solutions and FETD solutions using 1000 time steps at three offsets are provided in Fig. 6. The relative errors of these two results present periodic oscillations after one second for three different offsets. However, this phenomenon is easy to explain. The numerical errors by spatial discretization and finite-element approximation are (almost) subtracted when computing the relative errors, so only the local truncation errors of time discretization in the BE scheme are remained, which show a cyclical pattern in Fig. 6. Both the results of E_x and E_z demonstrate the good accuracy of our finite element based rational Krylov method for multi-source time-domain CSEM modelling.

Timings and efficiency

The multi-source CSEM problems can be modeled for each EM source by applying the rational Krylov method with a single vector, meanwhile they can also be solved all at once using block Krylov method, as discussed in the methodology section. We compare the consuming time for the three BE schemes in FETD modelling with both single-vector rational Krylov approximation and block Krylov approximation, which is shown in Table 1. Here only the time discretization in BE scheme (i.e., eq. (15.)) and rational Arnoldi approximation (i.e., Algorithm 1) are included in the timings. We choose the BE scheme with 1000 steps as the baseline and set its relative efficiency to one. Table 1 shows that block rational Krylov method is about 48% faster than single-vector rational Krylov method. Moreover, block rational Krylov method is 11.33 times faster than the BE scheme with 1000 time steps.

3.2 A synthetic 3D hydrocarbon reservoir model with seafloor bathymetry

To further reveal the ability and flexibility of block rational Krylov method for solving the real-world problem with complicated electric interfaces inside the earth, meanwhile to fully assess the performance of block method, we conduct numerical experiments using a 3D hydrocarbon reservoir model with significant seafloor bathymetry. Fig. 7 shows the seafloor bathymetry, EM sources and receivers in this model. We assume 45 transmitting sources distributed along three lines with an interval of 1000 m. The transmitting sources are about 50 m above the seafloor. The

survey lines are located at the seafloor parallel with the transmitting sources. On each line, EM receivers are laid along the seafloor every 100 meters, from -4000 m to 4000 m, totally 243 stations. The resistive hydrocarbon reservoir is $3000\text{ m} \times 2000\text{ m} \times 200\text{ m}$ in the x -, y -, and z -directions, while its center is located at [0, 0, 2000] m. The conductivities of air, seawater, sediments and the hydrocarbon reservoir are set to 10^{-8} , 3.33, 1.43 and 0.005 S/m respectively.

For the 3D hydrocarbon reservoir model, the outer boundary of the grid is empirically set 50 km from the center of the model, as that for the layered seafloor model. The maximum rate for element growth is 1.4 for meshing all the subdomains. For elements close to the transmitting sources, the minimum element size is chosen to be 1 m, while it is 3 m for those near the receivers. The seafloor bathymetry is described by a three-dimensional surface with a grid space of about 100 m, and no explicit constraints on element sizes are imposed. As a result, the modelling domain is divided into 692,221 tetrahedral elements by 117,052 nodes and 810,100 edges. The cross sections of the final tetrahedral grid are shown in Fig. 8(a) and Fig. 8(b).

The amplitude versus offset plots

Fig. 9 shows the inline component of electric field computed by the block rational Krylov method, where only the electric fields at inline receivers are plotted for each line. Electric fields are shown as “amplitude versus offset” plots, i.e., the absolute value of E_x field of 81 receivers in each line for 7 time channels logarithmically distributed in $[10^{-2}, 10^2]$ s are plotted versus their x coordinate. One can clearly

observe that E_x field shows a maximum when they are closing to the sources due to the strong effect of the EM transmitters. As a result of the influences of the energy of air wave ([Constable and Weiss, 2006](#)), there are large changes in the slope of the plots especially at the amplitudes from 4×10^{-11} V/m to 2×10^{-9} V/m. The electric field is very small at late time channels (e.g., the lowest two line plots of each subfigure in Fig. 9). In addition, they are not smooth horizontally for adjacent receivers. This can be easily explained as the result of the difference of their vertical locations. In fact, all the transmitters keep almost a constant distance above the interface (i.e., bathymetry, and the receivers) of seawater and sediment layer in our models, therefore the non-smooth phenomenon should be considered as the effect of bathymetry.

Comparison between rational Krylov solutions and BE solutions

Fig. 10 compares the EM responses by the block rational Krylov method and FETD method using BE scheme with 1000 time steps for each line, where there are 15 sources and 81 receivers. We can easily see that the relative differences for most transmitter and receiver pairs are less than 1%, except several very early time channels (i.e., from 0.01 s to 0.04 s). We examine these simulation results carefully and find that all the larger differences (still less than 5%) occur only at very short offsets (a few hundred meters near the sources). As the EM field diffuses to short offsets faster and there are no stable stages like that for longer offsets (e.g., 2 km to 6 km in Fig. 5), so we argue that smaller time steps at early times are necessary by BE scheme for this model. Similar periodic oscillations of relative differences are

presented for this model due to the remained truncation errors of the BE scheme. In general, the block rational Krylov method with only 40 rational Arnoldi iterations has accuracy as good as the FETD method using 1000 time steps for the complicated model.

The anomaly pseudo-sections

CSEM is an EM exploration method that measures total EM field rather than the secondary field. Furthermore, the EM fields present strong attenuation in the seawater and sediments which are both high conductive medium, particularly for long offsets. These two factors make the effect of hydrocarbon reservoir very difficult to be recognized in the plots of absolute scale (i.e., Fig. 9). The significant relief of the sediments even brings us more trouble. For these reasons, the anomaly pseudo-sections used by [Key and Oval \(2011\)](#) for frequency-domain CSEM problems are adopted here to identify the anomaly. The anomaly signal is defined as

Anomaly = $\frac{\mathbf{E}_{\text{reservoir}} - \mathbf{E}_{\text{background}}}{\mathbf{E}_{\text{background}}}$. Therefore, the background responses without the 3D hydrocarbon reservoir are then computed with our block rational Krylov method. For different time channels, the relative differences (i.e., the anomaly signal) of electric field with and without the reservoir are plotted, as shown in Fig. 11, where the x -axis is for the source-receiver midpoint, while the y -axis is for the source-receiver offset. We can see that the peak signals of the 3D reservoir occur at the offset about 3 km to 5 km. The maximum anomalies are about 10% to 15% for the early and middle time channels (see Fig. 11(a) and Fig. 11(b)), while they are below 5% for the late time

channels (see Fig. 11(d)). For the 3D hydrocarbon reservoir model shown in Fig. 7, the electric currents flow less vertically to the resistive hydrocarbon reservoir. The currents channeling effect leads to the increase of inline electric field, which is proved by the positive anomaly in Fig. 11.

Timings and efficiency

We benchmark the block rational Krylov method against single-vector rational Krylov method and FETD method using three BE schemes for 5, 15, 25, 35 and 45 sources separately, to demonstrate the speedup and memory requirements of block method for different number of sources. Table 2 gives the elapsed time of FETD method using three BE schemes, single-vector rational Krylov method and our block rational Krylov method. The speedup ratio is calculated by dividing the run time of the three BE schemes and two rational Krylov methods by that of the BE scheme using 1000 time steps. We can find that the efficiency of BE scheme increases if less time steps are carried out, meanwhile the elapsed time is almost proportional to the number of time steps. This is because only a few matrix decompositions are carried out in the advance of the EM solution, so the forward and backward substitutions for each time step are almost the most expensive tasks for multi-source problems. The simple repetition of single-vector method is also linear in time complexity, while the time cost for block method are approximately proportional to $ns^{1.5}$, which indicates that the block method may slow down with increasing number of sources, as discussed in the Section 2.5. However, the block method is still 26% faster (in the

worst case for our model) than the single-vector method for 45 sources. Considering the block method can produce equivalent accuracy with FETD using 1000 steps, as proved in Fig. 10, and the similar block Krylov iterative solvers can usually achieve a speedup between 1.5-fold and 2.0-fold (e.g., [Puzyrev and Cela, 2015](#)), this improvement is very significant and useful. The memory usage of the block Krylov method for different number of sources is reported in Table 3. A linear increase of the memory requirement with the number of sources ns is observed. This is due to the fact that the block basis $\mathbf{V}_{m+1} := [\mathbf{v}_1, \mathbf{v}_2, \dots, \mathbf{v}_{m+1}]$ requires the storage of $(m+1)ns$ single vectors and, together with the memory requirement for storing the matrix factorizations (that is independent of ns), these vectors dominate the memory foot-print.

4 CONCLUSION

We developed an efficient block rational Krylov forward solver for 3D time-domain CSEM modelling with unstructured tetrahedral grids. The rational Krylov method computes the efficient approximations to the electric field from a rational Krylov space without time-stepping, therefore avoids the common issues about designing the optimal time steps. Moreover, the rational approximations are implicit essentially, thus this remarkable property makes them suitable for handling the stiffness EM modelling problems just like the implicit time-stepping methods. By incorporating an exponential weight to the approximation error, we can obtain desired numerical accuracy with only 40 optimized shifts and thereby reduce the number of

linear system solves. Compared to the single-vector rational Krylov method, the proposed block technique takes advantage of the BLAS-3 functions for matrix-vector operations during the Arnoldi process with better memory efficiency. Numerical experiments verify the effectiveness and stability of the rational Krylov method and demonstrate that it can obtain equivalent accuracy with the backward Euler scheme using up to 1000 time steps but at a lower computational cost. If implemented the EM forward modeling with data domain decomposition by dividing all the sources into smaller groups and distributing the computation tasks over multiple processes, the block Krylov method could be very useful for problems with hundreds of sources. Our research indicates that the block rational Krylov method is a very promising choice for TDEM modelling.

ACKNOWLEDGEMENTS

We are grateful to the editor Dr. U. Weckmann and two reviewers Dr. D. Avdeev and Dr. V. Puzyrev for their constructive suggestions and comments that improved the clarity of the paper. This work is financially supported by the Key Program of National Natural Science Foundation of China (41530320), the Strategic Priority Research Program of the Chinese Academy of Sciences (XDA14020102), National Natural Science Foundation of China (41774125), and the Key National Research Project of China (2017YFC0601900, 2016YFC0303100). The work of S. Güttel has been supported by Engineering and Physical Sciences Research Council grant EP/N509565/1. C. Qiu is supported by China Scholarship Council (201706170179)

for one year of study at Oregon State University.

REFERENCES

- Amestoy, P.R., Guermouche, A., L'Excellent, J.-Y. & Pralet, S., 2006. Hybrid scheduling for the parallel solution of linear systems, *Parallel computing*, **32**(2), 136-156.
- Anderson, W.L., 1983. Fourier cosine and sine transforms using lagged convolutions in double-precision (subprograms DLAGFO/DLA/GF1), *US Geol. Surv. Open-file rep.*, 83-320.
- Ascher, U.M. & Petzold, L.R., 1998, *Computer methods for ordinary differential equations and differential-algebraic equations*, SIAM.
- Berljafa, M., Elsworth, S. & Güttel, S., 2014. A Rational Krylov Toolbox for MATLAB, *MIMS EPrint 2014.56, School of Mathematics, The University of Manchester, UK.*
- Börner, R.U., 2010. Numerical modelling in geo-electromagnetics: advances and challenges, *Surv. Geophys.*, **31**(2), 225-245.
- Börner, R.U., Ernst, O.G. & Güttel, S., 2015. Three-dimensional transient electromagnetic modelling using Rational Krylov methods, *Geophys. J. Int.*, **202**(3), 2025-2043.
- Börner, R.U., Ernst, O.G. & Spitzer, K., 2008. Fast 3-D simulation of transient electromagnetic fields by model reduction in the frequency domain using Krylov subspace projection, *Geophys. J. Int.*, **173**(3), 766-780.

- Cai, H.Z., Hu, X.Y., Xiong, B. & Zhdanov, M.S., 2017. Finite-element time-domain modeling of electromagnetic data in general dispersive medium using adaptive Padé series, *Comput. Geosci.*, **109**, 194-205.
- Chew, W.C., 1995, *Waves and fields in inhomogeneous media*, IEEE press.
- Commer, M. & Newman, G., 2004. A parallel finite-difference approach for 3D transient electromagnetic modeling with galvanic sources, *Geophysics*, **69**(5), 1192-1202.
- Connell, D. & Key, K., 2013. A numerical comparison of time and frequency-domain marine electromagnetic methods for hydrocarbon exploration in shallow water, *Geophys. Prospect.*, **61**(1), 187-199.
- Constable, S., 2010. Ten years of marine CSEM for hydrocarbon exploration, *Geophysics*, **75**(5), A67-A81.
- Constable, S. & Weiss, C.J., 2006. Mapping thin resistors and hydrocarbons with marine EM methods: Insights from 1D modeling, *Geophysics*, **71**(2), G43-G51.
- Cox, L.H., Wilson, G.A. & Zhdanov, M.S., 2010. 3D inversion of airborne electromagnetic data using a moving footprint, *Explor. Geophys.*, **41**(4), 250-259.
- Danielsen, J.E., Auken, E., Jørgensen, F., Søndergaard, V. & Sørensen, K.I., 2003. The application of the transient, electromagnetic method in hydrogeophysical surveys, *J. Appl. Geophys.*, **53**(4), 181-198.

- Druskin, V. & Knizhnerman, L., 1994. Spectral approach to solving three-dimensional Maxwell's diffusion equations in the time and frequency domains, *Radio Sci.*, **29**(4), 937-953.
- Druskin, V., Knizhnerman, L. & Zaslavsky, M., 2009. Solution of large scale evolutionary problems using rational Krylov subspaces with optimized shifts, *SIAM J. Sci. Comput.*, **31**(5), 3760-3780.
- Druskin, V., Lieberman, C. & Zaslavsky, M., 2010. On adaptive choice of shifts in rational Krylov subspace reduction of evolutionary problems, *SIAM J. Sci. Comput.*, **32**(5), 2485-2496.
- Druskin, V.L. & Knizhnerman, L.A., 1988. Spectral differential-difference method for numeric solution of three-dimensional nonstationary problems of electric prospecting, *Izvestiya, Solid Earth Physics*, **24**(8), 641-648.
- Du Fort, E.C. & Frankel, S.P., 1953. Stability conditions in the numerical treatment of parabolic differential equations, *Mathematical Tables and Other Aids to Computation*, **7**(43), 135-152.
- Farquharson, C.G. & Oldenburg, D.W., 1993. Inversion of time-domain electromagnetic data for a horizontally layered Earth, *Geophys. J. Int.*, **114**(3), 433-442.
- Fitterman, D.V. & Stewart, M.T., 1986. Transient electromagnetic sounding for groundwater, *Geophysics*, **51**(4), 995-1005.
- Fountain, D., Smith, R., Payne, T. & Limieux, J., 2005. A helicopter time-domain EM

- system applied to mineral exploration: System and data, *First Break*, **23**(1), 73-78.
- Frommer, A., Güttel, S. & Schweitzer, M., 2014. Efficient and stable Arnoldi restarts for matrix functions based on quadrature, *SIAM J. Matrix Anal. Appl.*, **35**(2), 661-683.
- Gallopoulos, E. & Saad, Y., 1989. On the parallel solution of parabolic equations. *in Proceedings of the 3rd international conference on Supercomputing*, pp. 17-28ACM.
- Güttel, S., 2013. Rational Krylov approximation of matrix functions: Numerical methods and optimal pole selection, *GAMM-Mitt*, **36**(1), 8-31.
- Haber, E., Ascher, U. & Oldenburg, D.W., 2002. 3D forward modelling of time domain electromagnetic data, *in 72nd Annual International Meeting*, pp. 641-644. SEG.
- Haber, E., Ascher, U.M. & Oldenburg, D.W., 2004. Inversion of 3D electromagnetic data in frequency and time domain using an inexact all-at-once approach, *Geophysics*, **69**(5), 1216-1228.
- Hoekstra, P. & Blohm, M.W., 1990. Case histories of time-domain electromagnetic soundings in environmental geophysics, *Geotechnical and environmental geophysics*, **2**, 1-16.
- Jahandari, H. & Farquharson, C.G., 2014. A finite-volume solution to the geophysical electromagnetic forward problem using unstructured grids, *Geophysics*, **79**(6),

E287-E302.

- Jang, H., Jang, H., Lee, K.H. & Kim, H.J., 2013. Step-off, vertical electromagnetic responses of a deep resistivity layer buried in marine sediments, *J. Geophys. Eng.*, **10**(2), 7.
- Kafri, U. & Goldman, M., 2005. The use of the time domain electromagnetic method to delineate saline groundwater in granular and carbonate aquifers and to evaluate their porosity, *J. Appl. Geophys.*, **57**(3), 167-178.
- Keating, P.B. & Crossley, D.J., 1990. The inversion of time-domain airborne electromagnetic data using the plate model, *Geophysics*, **55**(6), 705-711.
- Key, K. & Ovall, J., 2011. A parallel goal-oriented adaptive finite element method for 2.5-D electromagnetic modelling, *Geophys. J. Int.*, **186**(1), 137-154.
- Knight, J.H. & Raiche, A.P., 1982. Transient electromagnetic calculations using the Gaver-Stehfest inverse Laplace transform method, *Geophysics*, **47**(1), 47-50.
- Li, J., Lu, X., Farquharson, C.G. & Hu, X., 2018. A finite-element time-domain forward solver for electromagnetic methods with complex-shaped loop sources, *Geophysics*, **83**(3), E117-E132.
- Li, J.H., Farquharson, C.G. & Hu, X.Y., 2016. Three effective inverse Laplace transform algorithms for computing time-domain electromagnetic responses, *Geophysics*, **81**(2), E113-E128.
- Li, J.H., Farquharson, C.G. & Hu, X.Y., 2017. 3D vector finite-element electromagnetic forward modeling for large loop sources using a total-field

- algorithm and unstructured tetrahedral grids, *Geophysics*, **82**(1), E1-E16.
- Liu, Y.H. & Yin, C.C., 2016. 3D inversion for multipulse airborne transient electromagnetic data, *Geophysics*, **81**(6), E401-E408.
- Moret, I. & Novati, P., 2004. RD-rational approximations of the matrix exponential, *Bit*, **44**(3), 595-615.
- Nédélec, J.-C., 1980. Mixed finite elements in R 3, *Numerische Mathematik*, **35**(3), 315-341.
- Newman, G.A., Hohmann, G.W. & Anderson, W.L., 1986. Transient electromagnetic response of a three-dimensional body in a layered earth, *Geophysics*, **51**(8), 1608-1627.
- Oldenburg, D.W., Haber, E. & Shekhtman, R., 2013. Three dimensional inversion of multisource time domain electromagnetic data, *Geophysics*, **78**(1), E47-E57.
- Oristaglio, M.L. & Hohmann, G.W., 1984. Diffusion of electromagnetic fields into a two-dimensional earth: A finite-difference approach, *Geophysics*, **49**(7), 870-894.
- Puzeyrev V, & Cela J M., 2015. A review of block Krylov subspace methods for multisource electromagnetic modelling. *Geophys. J. Int.*, **202**(2): 1241-1252.
- Ren, X.Y., Yin, C.C., Liu, Y.H., Cai, J., Wang, C. & Ben, F., 2017. Efficient Modeling of Time-domain AEM using Finite-volume Method, *J. Environ. Eng. Geophys.*, **22**(3), 267-278.
- Ren, Z.Y., Kalscheuer, T., Greenhalgh, S. & Maurer, H., 2013. A goal-oriented

- adaptive finite-element approach for plane wave 3-D electromagnetic modelling, *Geophys. J. Int.*, **194**(2), 700-718.
- Ruhe, A., 1994. Rational Krylov algorithms for nonsymmetric eigenvalue problems. *in Recent advances in iterative methods*, pp. 149-164. Springer.
- Saad, Y., 1992. Analysis of some Krylov subspace approximations to the matrix exponential operator, *SIAM J. Numer. Anal.*, **29**(1), 209-228.
- Saad, Y., 2003, *Iterative methods for sparse linear system*, SIAM.
- Schmucker, U. & Weidelt, P., 1975. Electromagnetic induction in the earth, *Lecture Notes, Aarhus Univ., Denmark*.
- Schulze, J., 2001. Towards a tighter coupling of bottom-up and top-down sparse matrix ordering methods, *Bit*, **41**(4), 800-841.
- Si, H., 2015. TetGen, a Delaunay-Based Quality Tetrahedral Mesh Generator, *ACM Trans. Math. Softw.*, **41**(2), 36.
- Stehfest, H., 1970. Algorithm 368 Numerical inversion of Laplace transforms [D5], *Commun. ACM*, **13**(1), 47-49.
- Um, E.S., Harris, J.M. & Alumbaugh, D.L., 2010. 3D time-domain simulation of electromagnetic diffusion phenomena: A finite-element electric-field approach, *Geophysics*, **75**(4), F115-F126.
- Van den Eshof, J. & Hochbruck, M., 2006. Preconditioning Lanczos approximations to the matrix exponential, *SIAM J. Sci. Comput.*, **27**(4), 1438-1457.
- Wang, T. & Hohmann, G.W., 1993. A finite-difference, time-domain solution for

- three-dimensional electromagnetic modeling, *Geophysics*, **58**(6), 797-809.
- Wright, D., Ziolkowski, A. & Hobbs, B., 2002. Hydrocarbon detection and monitoring with a multicomponent transient electromagnetic (MTEM) survey, *The Leading Edge*, **21**(9), 852-864.
- Yang, D., Oldenburg, D.W. & Haber, E., 2013. 3-D inversion of airborne electromagnetic data parallelized and accelerated by local mesh and adaptive soundings, *Geophysical Journal International*, **196**(3), 1492-1507.
- Yang, D.K. & Oldenburg, D.W., 2012. Three-dimensional inversion of airborne time-domain electromagnetic data with applications to a porphyry deposit, *Geophysics*, **77**(2), B23-B34.
- Yin, C.C., Qi, Y.F. & Liu, Y.H., 2016a. 3D time-domain airborne EM modeling for an arbitrarily anisotropic earth, *J. Appl. Geophys.*, **131**, 163-178.
- Yin, C.C., Qi, Y.F., Liu, Y.H. & Cai, J., 2016b. 3D time-domain airborne EM forward modeling with topography, *J. Appl. Geophys.*, **134**, 11-22.
- Zaslavsky, M., Druskin, V. & Knizhnerman, L., 2011. Solution of 3D time-domain electromagnetic problems using optimal subspace projection, *Geophysics*, **76**(6), F339-F351.

LIST OF FIGURES

Figure 1. Rational Arnoldi approximation errors with 2 distinct shift parameters which repeat 20 times for the desired time interval $t=[10^{-2}, 10^2]$ s. (a) The exponential weight function; (b) Arnoldi error and orthogonal projection of the rational Arnoldi approximations.

Figure 2. Time-stepping sizes as the function of EM diffusion time for the three BE schemes. The total number of time steps are 1000, 595 and 200 respectively.

Figure 3. Layered seafloor model with CSEM transmitters and receivers. The three short lines are electric-dipole sources. The eight circles are receivers on the seafloor.

Figure 4. Cross section of the tetrahedral grid at $y=0$ m for the layered seafloor model shown in Fig. 3. The elements in green represent sea water, while grids in blue and red are air and seabed sediments respectively.

Figure 5. Comparison of inline electric field and vertical electric field computed by block rational Krylov method against 1D semi-analytic solutions at three offsets. (a) and (c) are E_x and E_z at the offset=2 km, 4 km, 6 km for the three sources shown in Fig. 3. The line plots are for 1D solutions, while the scatters are the block rational Krylov solutions. (b) and (d) are the relative errors for E_x and E_z in percentage.

Figure 6. The relative errors between block rational Krylov solutions and FETD solutions using 1000 time steps for the layered seafloor model at three offsets. (a) and (b) are for E_x and E_z respectively.

Figure 7. Perspective of the seafloor bathymetry, EM sources and receivers for the 3D hydrocarbon reservoir model. The grey cube is the resistive hydrocarbon reservoir. The red short lines denote the EM sources, and the blue dots are the EM receivers. The black dots and segments are generated by the topography data which describe the bathymetry (shown as grey interface) and control the generation of the grid.

Figure 8. The cross sections of the unstructured tetrahedral grid discretization of the 3D hydrocarbon reservoir model with seafloor bathymetry. The grids in green are for sediments, while the grids in red are for the resistive hydrocarbon reservoir. The grids in blue are elements near the EM receivers. The sea water layer has been omitted in the plots. (a) Clip at $x=0$ m; (b) Clip at $y=0$ m.

Figure 9. Inline electric field responses for the complex 3D hydrocarbon reservoir model with seafloor bathymetry. EM responses for 7 time channels logarithmically distributed in $[10^{-2}, 10^2]$ s are plotted. Each peak in the line plots is for one transmitting source. (a) E_x for Line 1; (b) E_x for Line 2; (c) E_x for Line 3.

Figure 10. The relative differences between block rational Krylov results and BE solutions with 1000 time steps for the 3D hydrocarbon reservoir model. The black solid lines indicate a relative difference of 5%. Only the inline responses are considered in the plots. (a) Line 1; (b) Line 2; (c) Line 3.

Figure 11. Inline electric field anomaly midpoint-offset sections for the 3D complicated model illustrated in Fig. 7 at four different times. The relative differences

of the electric field solutions with and without the hydrocarbon reservoir are plotted horizontally at the midpoint of the source–receiver pairs and vertically at the source–receiver offset.

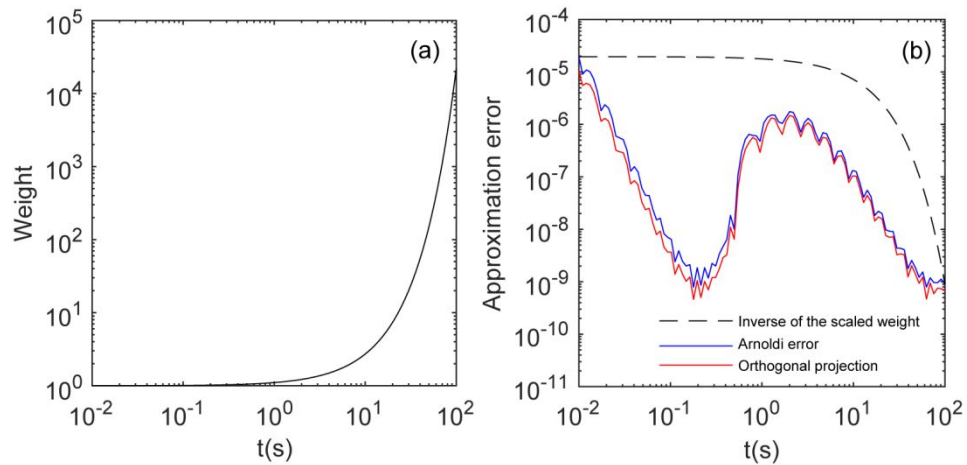


Figure 1. Rational Arnoldi approximation errors with 2 distinct shift parameters

which repeat 20 times for the desired time interval $t=[10^{-2}, 10^2]$ s. (a) The exponential weight function; (b) Arnoldi error and orthogonal projection of the rational Arnoldi approximations.

138×67 mm (300×300 DPI)

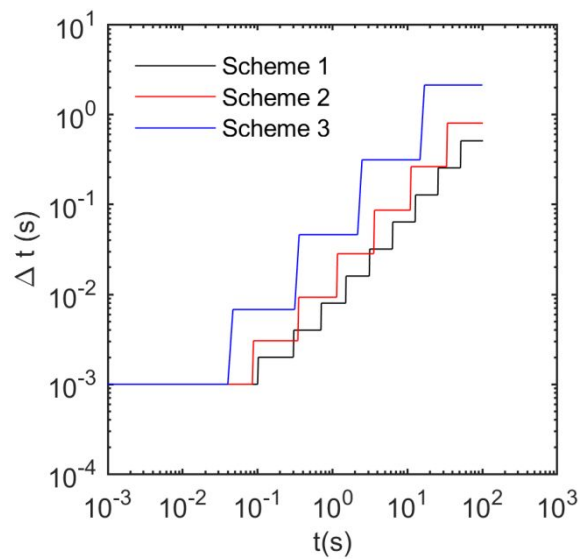


Figure 2. Time-stepping sizes as the function of EM diffusion time for the three BE schemes. The total number of time steps are 1000, 595 and 200 respectively.

75×73 mm (300×300 DPI)

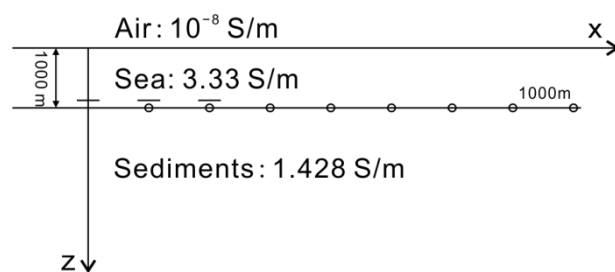


Figure 3. Layered seafloor model with CSEM transmitters and receivers. The three short lines are electric-dipole sources. The eight circles are receivers on the seafloor.

80×34 mm (300×300 DPI)

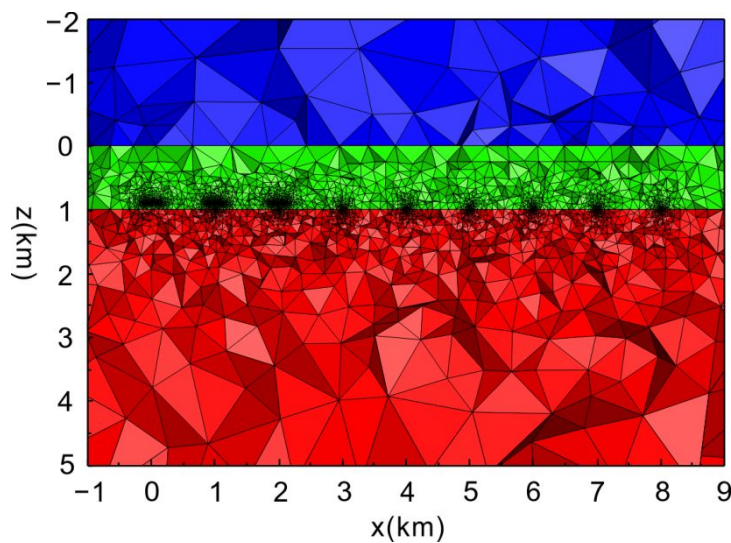


Figure 4. Cross section of the tetrahedral grid at $y=0$ m for the layered seafloor model shown in Fig. 3. The elements in green represent sea water, while grids in blue and red are air and seabed sediments respectively.

94×69 (300×300 DPI)

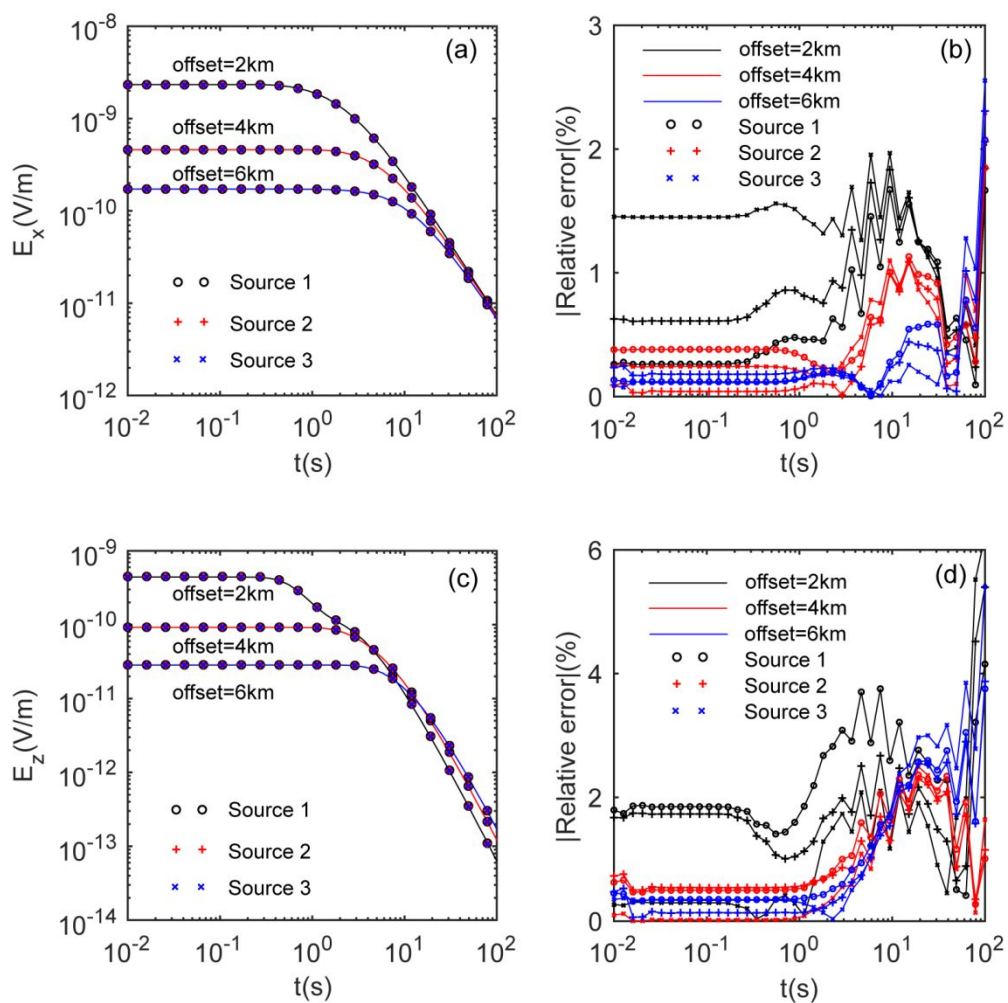


Figure 5. Comparison of inline electric field and vertical electric field computed by block rational Krylov method against 1D semi-analytic solutions at three offsets. (a) and (c) are E_x and E_z at the offset=2 km, 4 km, 6 km for the three sources shown in Fig. 3. The line plots are for 1D solutions, while the scatters are the block rational Krylov solutions. (b) and (d) are the relative errors for E_x and E_z in percentage.

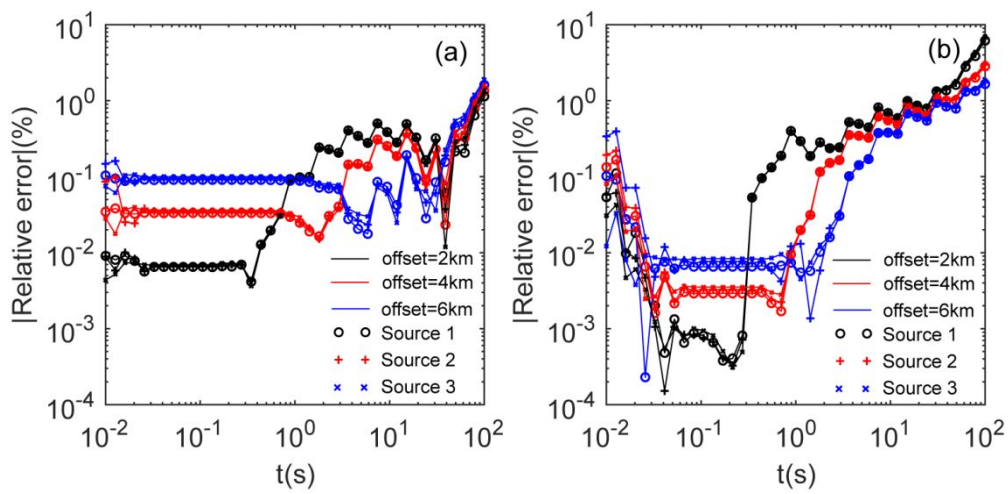


Figure 6. The relative errors between block rational Krylov solutions and FETD solutions using 1000 time steps for the layered seafloor model at three offsets. (a) and (b) are for E_x and E_z respectively.

132×64 mm (300×300 DPI)

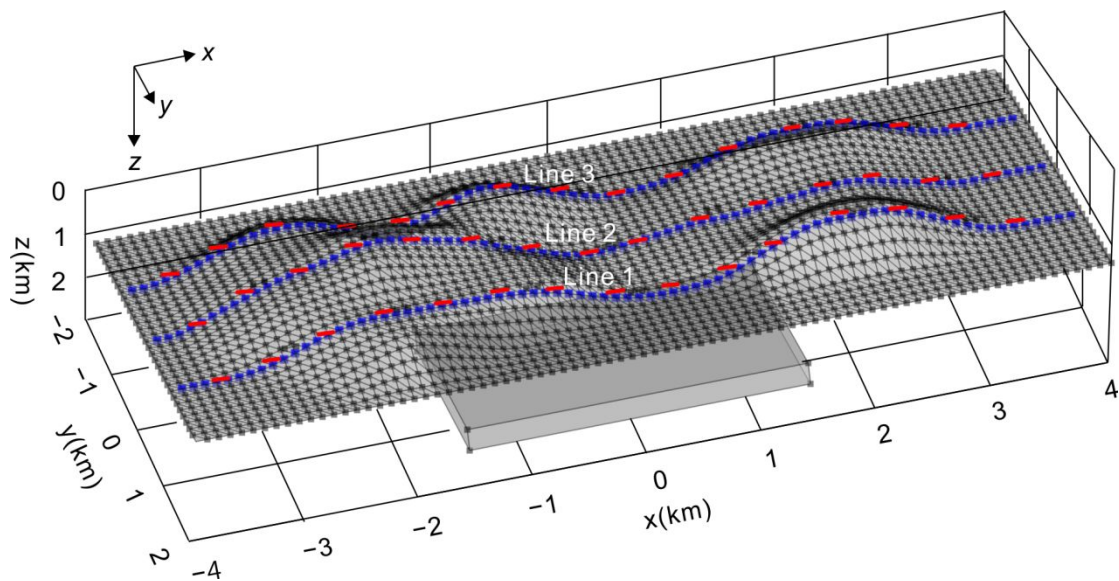


Figure 7. Perspective of the seafloor bathymetry, EM sources and receivers for the 3D hydrocarbon reservoir model. The grey cube is the resistive hydrocarbon reservoir. The red short lines denote the EM sources, and the blue dots are the EM receivers. The black dots and segments are generated by the topography data which describe the bathymetry (shown as grey interface) and control the generation of the grid.

158×81 mm (300×300 DPI)

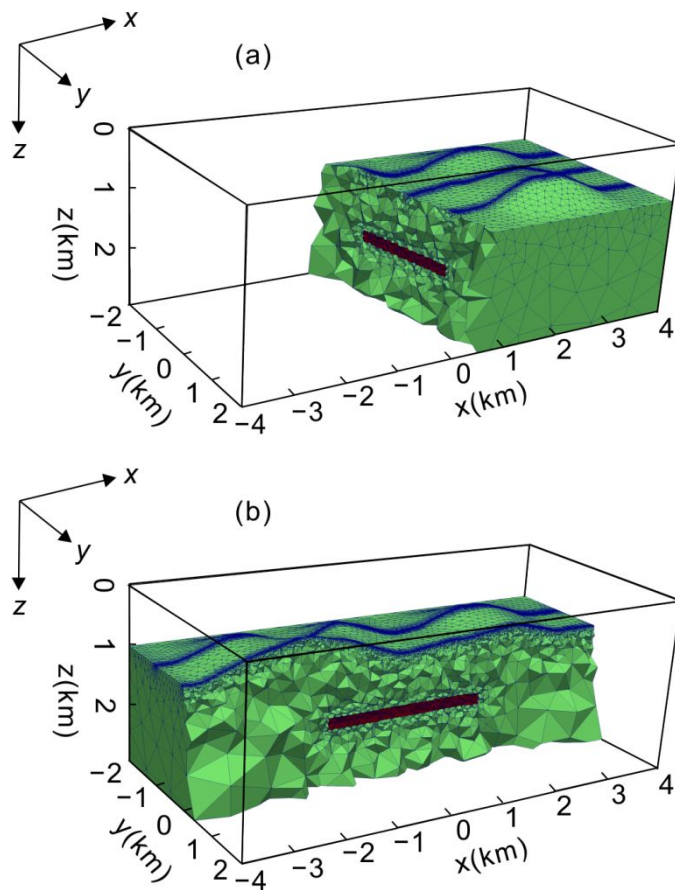


Figure 8. The cross sections of the unstructured tetrahedral grid discretization of the 3D hydrocarbon reservoir model with seafloor bathymetry. The grids in green are for sediments, while the grids in red are for the resistive hydrocarbon reservoir. The grids in blue are elements near the EM receivers. The sea water layer has been omitted in the plots. (a) Clip at $x=0$ m; (b) Clip at $y=0$ m.

93×116 mm (300×300 DPI)

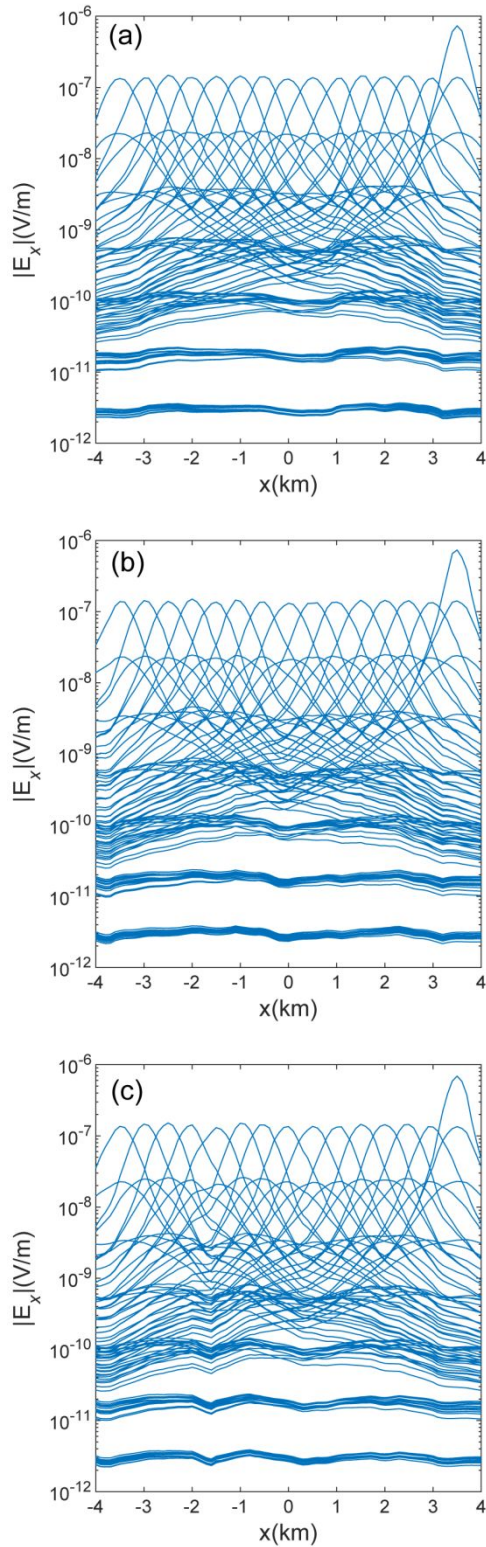


Figure 9. Inline electric field responses for the complex 3D hydrocarbon reservoir model with seafloor bathymetry. EM responses for 7 time channels logarithmically distributed in $[10^{-2}, 10^2]$ s are plotted. Each peak in the line plots is for one transmitting source. (a) E_x for Line 1; (b) E_x for Line 2; (c) E_x for Line 3.

80×240 mm (300×300 DPI)

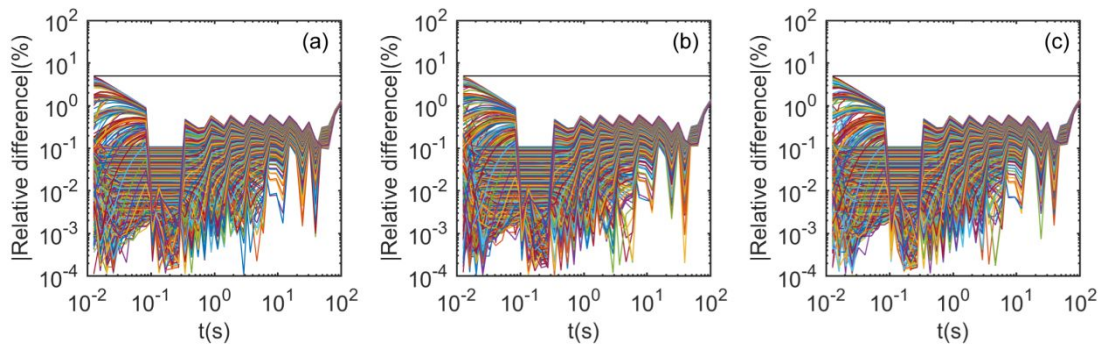


Figure 10. The relative differences between block rational Krylov results and BE solutions with 1000 time steps for the 3D hydrocarbon reservoir model. The black solid lines indicate a relative difference of 5%. Only the inline responses are considered in the plots. (a) Line 1; (b) Line 2; (c) Line 3.

180×60 mm (300×300 DPI)

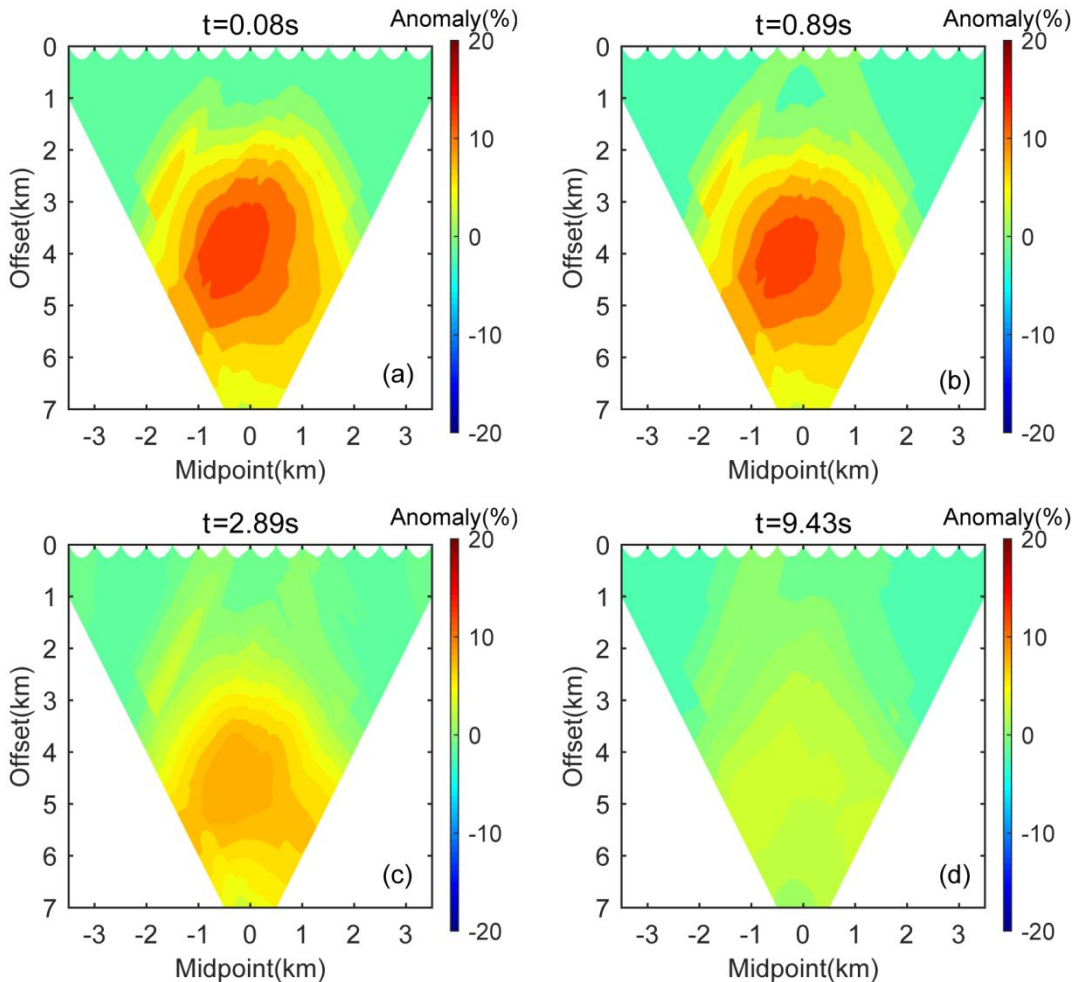


Figure 11. Inline electric field anomaly midpoint-offset sections for the 3D complicated model illustrated in Fig. 7 at four different times. The relative differences of the electric field solutions with and without the hydrocarbon reservoir are plotted horizontally at the midpoint of the source–receiver pairs and vertically at the source–receiver offset.

150×133 mm (300×300 DPI)

LIST OF TABLES

Table 1. Elapsed time and efficiency for the layered-earth seafloor model shown in Fig. 3.

Table 2. Comparison of computational time of forward modelling using FETD method using 3 BE schemes, single-vector rational Krylov method and block rational Krylov method for the 3D hydrocarbon reservoir model with seafloor bathymetry shown in Fig. 7. Numerical experiments are performed for different number of sources.

Table 3. Memory usage of block rational Krylov method for different number of sources.

Table 1. Elapsed time and efficiency for the layered-earth seafloor model shown in Fig. 3.

Method	Elapsed time	Relative efficiency
FETD Scheme 1	922 s	1.00
FETD Scheme 2	546 s	1.69
FETD Scheme 3	202 s	4.56
Single-vector rational Krylov	Solving the initial vectors	4.5 s
	Construction of rational Krylov basis	114.6 s
	Evaluation of electric solutions	1.5 s
Block rational Krylov	Solving the initial vectors	4.5 s
	Construction of rational Krylov basis	75.2 s
	Evaluation of electric solutions	1.7 s

Table 2. Comparison of computational time of forward modelling using FETD method using 3 BE schemes, single-vector rational Krylov method and block rational Krylov method for the 3D hydrocarbon reservoir model with seafloor bathymetry shown in Fig. 7. Numerical experiments are performed for different number of sources.

Method Number of sources \	FETD Scheme 1	FETD Scheme 2	FETD Scheme 3	Single-vector rational Krylov	Block rational Krylov	Relative efficiency
$ns=5$	100.0 min	67.0 min	20.5 min	17.5 min	8.8 min	1.00/1.49/4.88/5.71/11.36
$ns=15$	334.5 min	176.0 min	58.5 min	52.4 min	25.3 min	1.00/1.90/5.72/6.38/13.22
$ns=25$	494.0 min	334.5 min	113.5 min	87.4 min	48.7 min	1.00/1.48/4.35/5.65/10.14
$ns=35$	648.0 min	409.0 min	160.0 min	122.2 min	82.8 min	1.00/1.58/4.05/5.30/7.83
$ns=45$	921.0 min	584.0 min	179.5 min	157.1 min	124.5 min	1.00/1.58/5.13/5.86/7.40

Table 3. Memory usage of block rational Krylov method for different number of sources.

Number of sources	Memory for the matrix factorization (in MB)	Memory for the basis vectors (in MB)	Total memory usage (in MB)
$ns=1$	5939	253	6272
$ns=5$	5939	1265	7271
$ns=15$	5939	3795	9772
$ns=25$	5939	6325	12374
$ns=35$	5939	8855	14892
$ns=45$	5939	11385	17395